Multiscale smoothed particle hydrodynamics model development for simulating preferential flow dynamics in fractured porous media

E. Shigorina[1*], F. Rüdiger[1], A. M. Tartakovsky[2], M. Sauter[1], and J. Kordilla[1]

[1]University of Goettingen, Dept. Applied Geology, 37077, Germany
[2]Computational Mathematics Group, Pacific Northwest National Laboratory, Richland, WA 99352, USA

Key Points:

- We developed a new SPH approach to study variably saturated flow in fractures adjacent to a porous matrix.
- We coupled the Navier–Stokes and Richards equations to study gravity-driven flow and matrix imbibition dynamics.
- We validated the model via laboratory experiments and study the effect of ponding on preferential flow dynamics in porous-fractured media.

[*]University of Goettingen, Dept. Applied Geology, 37077, Germany

Corresponding author: Elena Shigorina, eshigor@gwdg.de

Abstract

We present our new multiscale pairwise-force smoothed particle hydrodynamics (PF-SPH) model for the characterization of flow in fractured porous media. The fully coupled multiscale PF-SPH model is able to simulate flow dynamics in a porous and permeable matrix and in adjacent fractures. Porous medium flow is governed by the volume-effective Richards equation, while the flow in fractures is governed by the Navier–Stokes equation. Flow from a fracture to the porous matrix is modeled by an efficient particle removal algorithm and a virtual water redistribution formulation to enforce mass and momentum conservation. The model is validated by (1) comparison to a finite element model (FEM) COMSOL for Richards-based flow dynamics in a partially saturated medium and (2) laboratory experiments to cover more complex cases of free-surface flow dynamics and imbibition into the porous matrix. For the laboratory experiments, Seeberger sandstone is used because of its well-known homogeneous pore space properties. The saturated hydraulic conductivity of the permeable matrix is estimated from a pore size and grain size distribution analysis. The developed PF-SPH model shows good correlation with the COMSOL model and all types of laboratory experiments.

We employ the proposed model to study preferential flow dynamics for different infiltration rates. Here, flow in fracture is associated with the term "preferential flow," providing rapid water transmission, while flow within the adjacent porous matrix enables only slow and diffuse water transmission. Depending on the infiltration rate and water inlet location, two cases can be distinguished: (1) immediate preferential/fracture flow or (2) delayed preferential flow. In the latter case, water accumulates at the surface first (ponding), then the fracture rapidly transmits water to the bottom system outlet. For the immediate fracture flow response, ponding only occurs once the fracture is fully saturated with water. In all cases, preferential flow is much more rapid than diffuse flow even under saturated porous medium conditions.

Furthermore, infiltration dynamics in rough fractures adjacent to an impermeable or permeable matrix for different infiltration rates are studied as well. The simulation results show a significant lag in arrival times for small infiltration rates when a permeable porous matrix is employed, rather than an impermeable one. For higher infiltration rates, water rapidly flows through the fracture to the system outlet without any significant delay in arrival times even in the presence of the permeable matrix. The analysis of the amount of water stored in permeable fracture walls and in a fracture void space shows that for small infiltration rates, most of the injected water is retarded within the porous matrix. Flow velocity is higher for large infiltration rates, such that most of the water flows rapidly to the bottom of the fracture with very little influence of matrix imbibition processes.

1 Introduction

Most consolidated porous rocks are and/or have been subject to tectonically induced stress fields, which lead to discontinuities within the porous matrix (Nelson, 2001). Naturally fractured porous media consist of pore networks and interconnected or isolated fractures. Here, we adopt the notion that large pores and crevices are associated with the term fractures and have dimensions of 1×10^{-4} m to 1×10^{-2} m (Fischer et al., 1998; Tsang & Tsang, 1987), while pore throats of the matrix have dimensions of 1×10^{-7} m to 1×10^{-5} m (Thoma et al., 1992). In this study *fractures* are large pores or crevices, with an aperture of more than 1.0 mm and dimensions of width and length that can exceed 10.0 mm. Furthermore, fractures have a much stronger anisotropic character compared to pores, i.e. their aperture is several orders of magnitude smaller then the other two dimensions (width and length). Apart from this classification and based on their genetic origin, fractures are associated with stress field changes, while pores (primary porosity) are commonly the result of sedimentation and consolidation processes of granular

media. In principle, fractures are considered fast flow and transport pathways (Zimmerman & Bodvarsson, 1996), however, under partial saturation conditions they can also impede flow (Wang & Narasimhan, 1985). Despite their importance for rapid transmission of water it should be noted that the bulk porosity of fractured-porous rocks is still dominated by the porous matrix (Singhal & Gupta, 2010). The strong contrasts in spatial scales between the fracture aperture, its in-plane dimensions and the pore throats of the matrix make the characterization of infiltration dynamics in fractured porous media difficult with most numerical approaches.

Flow in partially saturated porous media is commonly described by the volume-averaged Richards (1931) equation. While it was originally developed for soil systems, the Richards equation is often applied to model flow in fractured systems (Heilweil et al., 2015; Therrien & Sudicky, 1996) when the fracture density is sufficiently high (or fracture apertures are rather small) and an representative elementary volume (REV) can be defined. Given the complexity of gravity-driven flow, many discrete flow and transport processes, including fingering, preferential flow pathway formation, meandering, and erratic flow mode dynamics (droplets and rivulets), cannot be described properly by the Richards equation.

The complexity of flow in fractured porous media is amongst others caused by the strong scale contrasts of the heterogeneity, i.e., the fracture thickness is associated with a much smaller scale than the fracture length. Furthermore, the scale contrast between porethroats of the matrix and the fracture scales make the characterization of infiltration dynamics in fractured porous media difficult or impossible with a discrete approach resolving the porous systems as well as the fracture. On the other hand, volume-effective solutions often neglect the effects of preferential flow paths and are commonly applied for large-scale characterization. Approaches based on dual-domain concepts (Nimmo, 2010; Germann et al., 2007) assume that the porous medium consists of two interacting regions, one of them associated with the fracture system, another one with the rock matrix, and hence can resolve the dualistic nature of such systems, though without any information about geometry or topology of the macropore system. (Semi-analytical solutions for preferential flows are commonly taking into consideration a single specific flow mode (droplets, rivulets, films) or transitions between them (Ghezzehei, 2004). However, For fractured systems the porous matrix plays an important role in the formation of fracture flows and can therefore not be neglected. Tokunaga and Wan (1997) demonstrated that adsorbed films are an important mechanism for unsaturated flow in fractures, and a fast flow process in contrast to diffuse flow in the porous matrix.

Preferential flow within the unsaturated (vadose) zone is known to strongly influence groundwater recharge, infiltration, and contaminant transport. The conditions under which preferential flow occurs and what the main controlling parameters are is still subject to debate for soil systems (Nimmo, 2010). Even less studies have focused on its occurrence in consolidated fractured systems. (Buscheck et al., 1991; Nitao, 1991) for example provide a criterion for critical fluxes that lead to preferential flow. They state that for infiltration rates smaller than the critical flux, diffuse/porous-medium flow dominates system the flow dynamics. For fluxes larger than the critical flux, fracture flow dominates.

For infiltration in soils various authors (Nimmo, 2010, 2012; Germann et al., 2007) demonstrated that preferential flow can occur under partially saturated conditions, in the absence of surface ponding or a fully saturated porous matrix, i.e. under non-equilibrium conditions.

Partially saturated flow in fractures is not well understood due to the uncertainty in generalizing flow processes, and scale effects, characterization of process parameters across scales, and the assessment of their relevance in the prediction of large-scale problems, such as the regional hydraulics of fault zones.

Therefore, we developed a multiscale smoothed particle hydrodynamics (SPH) model to study conditions that lead to preferential flow in partially saturated porous-fractured systems. The pairwise-force smoothed particle hydrodynamics (PF-SPH) is implemented within the Large-scale Atomic/Molecular Massively Parallel Simulator (LAMMPS) (Plimpton, 1995; Kordilla et al., 2017). The model is based on a PF-SPH discretization of the Navier–Stokes (NS) equation and can efficiently model flow through fractures or fracture networks and adequately recover all relevant flow dynamics, including the effects of free surface flows and surface tension (A. Tartakovsky & Meakin, 2005; Kordilla J., 2013; Kordilla et al., 2017; Shigorina et al., 2017, 2019). However, in porous-fractured systems, the porous and/or permeable matrix represents an important storage compartment and influences flow dynamics within the highly permeable fractures. This is the first model that tightly couples the Navier-Stokes flow in a fracture with the continuum (Richards) model of flow in the adjacent matrix. Most of the existing subsurface codes treat both fractures and matrix as continuums or a dual-continuum. These models cannot describe the complex physics of flow in fractures, e.g., complex infiltration dynamics in the unsaturated zone at Yucca Mountain (Doughty, 1999; C. & S., 1998). Such approaches are based on the assumption that the system is well mixed within the elementary representative volume. Our approach does not rely on this assumption for flow in fracture – therefore, it can be used to: (1) test the limits of applicability of the models using continuum description of fractured porous medium; (2) study the effect of boundary conditions on flow regimes in fractures; and (3) potentially improve continuum models.

The PF-SPH-LAMMPS code has been extensively validated (Kordilla J., 2013; Kordilla et al., 2017; Shigorina et al., 2017) for simulating gravity-driven free-surface and fracture flows under dynamic wetting conditions. The newly developed code for simulating flow in porous media, on and across the fracture–matrix interface is validated against a finite-element COMSOL model and small-scale laboratory experiments.

In order to study preferential flow dynamics, we investigate for which infiltration rates fracture flow dominates and for which rates diffuse flow dominates. The latter scenario occurs when a fracture acts as a flow barrier and hence causes ponding. Finally, we study the influence of fracture wall permeability and storage properties of the porous matrix on the arrival times for different infiltration rates. We consider two types of rough fractures: (1) a fracture with a permeable adjacent matrix and (2) a fracture with an impermeable adjacent matrix. Each fracture has two surfaces with a width of 50.0 mm, a length of 100.0 mm, and a thickness of 10.0 mm that are separated by a 2.0 mm aperture. The fracture roughness is characterized by the Hurst exponent ζ (Bouchaud et al., 1990; Shigorina et al., 2019) and an initial maximum value Δ for random displacement from a planar surface.

2 Governing Equations and the PF-SPH Method

In the following, we introduce the governing partial differential equations (PDEs) for the studied system and provide an overview of the employed SPH model, including SPH discretization of the PDEs and boundary conditions, as well as the coupling procedure between the NS and Richards domains. The more detailed information about fundamentals of SPH method is provided in Appendix A.

Assuming that the air phase is connected and has constant pressure (which we set here to zero) the partially saturated flow in porous media is commonly modeled using the Richards equation and suitable pressure–saturation relationships. In our model we use the mixed form of the Richards equation (Celia et al., 1990; Cockett, 2013)

$$\frac{\partial \Theta(\psi)}{\partial t} = (C_m + \rho \mathbf{g} S e S_s)\frac{\partial \psi}{\partial t} = \nabla \cdot \mathbf{K}_s k_r(\psi) \nabla \psi + \frac{\partial K(\psi)}{\partial z}, \tag{1}$$

where Θ is the water content, $\psi(x,t) = \int dP/rho$ is the pressure head (the integral is taken from an arbitrarily chosen reference pressure $P_r$to the pressure P at the point x),

$\mathbf{K}_s$ is the saturated hydraulic conductivity, S_s is the specific storage coefficient, ρ is the water density, and $\mathbf{g}$ is the gravitational acceleration. The parameters C_m (specific moisture capacity), S_e (effective saturation), and k_r (relative hydraulic conductivity) are derived from the van Genuchten relationships (van Genuchten, 1980):

$$Se = \begin{cases} \frac{1}{\left[1+|\alpha\psi|^n\right]^m} & \text{if } \psi < 0 \\ 1 & \text{if } \psi \geq 0 \end{cases}, \tag{2a}$$

$$k_r = \begin{cases} Se^{0.5}\left[1-\left(1-Se^{\frac{1}{m}}\right)^m\right]^2 & \text{if } \psi < 0 \\ 1 & \text{if } \psi \geq 0 \end{cases}, \tag{2b}$$

$$C_m = \begin{cases} \frac{\alpha m}{1-m}(\Theta_s - \Theta_r) Se^{\frac{1}{m}}\left(1-Se^{\frac{1}{m}}\right)^m & \text{if } \psi < 0 \\ 0 & \text{if } \psi \geq 0 \end{cases}. \tag{2c}$$

Here, α and n are the van Genuchten parameters, $m = 1 - 1/n$, and Θ_s and Θ_r are the saturated and residual liquid volume fractions, respectively.

The free-surface fracture flow is governed by the continuity equation,

$$\frac{d\rho}{dt} = -\rho(\nabla \cdot \mathbf{v}), \tag{3}$$

and the momentum conservation equation,

$$\frac{d\mathbf{v}}{dt} = -\frac{1}{\rho}\nabla P + \frac{\mu}{\rho}\nabla^2\mathbf{v} + \mathbf{g}, \tag{4}$$

where ρ is the fluid density, $\mathbf{v}$ is the fluid velocity, P is the fluid pressure in the fracture, μ the viscosity, and $\mathbf{g}$ is the gravitational acceleration. At the water–air interface, the Young–Laplace boundary condition

$$P\mathbf{n} = \boldsymbol{\tau}_w \cdot \mathbf{n} + S\sigma\mathbf{n}, \tag{5}$$

and the continuity condition

$$(\mathbf{v} - \mathbf{v}_b) \cdot \mathbf{n} = 0, \tag{6}$$

are enforced. Here, $\boldsymbol{\tau}_w = [\mu(\nabla\mathbf{v} + \nabla\mathbf{v}^{\mathrm{T}})]$ is the viscous stress tensor, S is the interface curvature, σ is the surface tension, and $\mathbf{v}_b$ is the boundary velocity, and $\mathbf{n}$ is the normal vector pointing away from the non-wetting phase.

The contact angle is prescribed at the water–air–solid contact line and the no-slip boundary condition at the boundary between the water and solid phases.

To complete the formulation, we note that the pressure in the partially saturated matrix also satisfies the Young-Laplace boundary condition, where S is the curvature of the water-air interface in the pores of the matrix.

To numerically solve these equations with the SPH method, we discretize the porous matrix with a set of solid particles and the fluid in the fracture with a set of fluid particles. The positions of solid particles are fixed, and their velocities are set to zero. The positions and velocities of fluid particles are found from the momentum conservation equation discretized with the weakly compressible pairwise SPH scheme (Morris et al., 1997; A. Tartakovsky & Meakin, 2005; Kordilla J., 2013; Kordilla et al., 2017):

$$\begin{aligned} \frac{d\mathbf{v}_i}{dt} = &-\sum_{j=1}^{N} m_j\left(\frac{P_j}{\rho_j^2} + \frac{P_i}{\rho_i^2}\right)\frac{\mathbf{r}_{ij}}{r_{ij}} \cdot \frac{dW(r_{ij},h)}{dr_{ij}} + \\ &2\mu\sum_{j=1}^{N} m_j \frac{\mathbf{v}_{ij}}{\rho_i\rho_j r_{ij}} \cdot \frac{dW(r_{ij},h)}{dr_{ij}} + \mathbf{g} + \frac{1}{m_i}\sum_{j=1}^{N}\mathbf{F}_{ij}\,, \end{aligned} \tag{7}$$

and

$$\frac{d\mathbf{r}_i}{dt} = \mathbf{v}_i, \tag{8}$$

where the summation is performed over all particles, including fluid and solid particles. In Eqs. (1)–(8), $\mathbf{r}_{ij} = \mathbf{r}_i - \mathbf{r}_j$ and $r_{ij} = |\mathbf{r}_i - \mathbf{r}_j|$, $m_i = m_j = m_0$ is the (constant) mass of particle i and j, ρ_j and P_j are the density and pressure, respectively, of the fluid carried by particle j, and h is the support range (or, so-called, *smoothing length*) of the kernel W. Fluid and solid particles are assumed to have the same mass, and ρ_i is computed for both fluid and solid particles as (Morris et al., 1997; A. Tartakovsky & Meakin, 2005)

$$\rho_i = \sum_{j=1}^{N} m_j W(\mathbf{r}_{ij}, h)\,. \tag{9}$$

The pressure of both fluid and solid particles is computed from the equation of state (Batchelor, 1967):

$$P_i = P_0\Big\{\Big(\frac{\rho_i}{\rho_0}\Big)^{\gamma} - 1\Big\}, \tag{10}$$

where

$$P_0 = \frac{c^2\rho_0}{\gamma}, \tag{11}$$

$\gamma = 7$, ρ_0 is the equilibrium particle density, and the speed of sound c is chosen such that the relative density fluctuation $|\delta\rho|/\rho$ is small (less than 3%) to approximate the behaviour of an incompressible fluid.

In Eqs. (15), (7), and (9), we use W in the form of a so-called "Wendland" kernel (Wendland, 1995):

$$W = \alpha_k \begin{cases} (1 - \frac{|\mathbf{r}|}{h})^3 & \text{if } 0 \le |\mathbf{r}| < h \\ \\ 0 & \text{if } |\mathbf{r}| \ge h \end{cases}, \tag{12}$$

where $\alpha_k = 168/16\pi h^3$.

The force $\mathbf{F}_{ij}$ in Eq. (7) is used to impose the Young–Laplace boundary condition. Following A. Tartakovsky and Meakin (2005); A. M. Tartakovsky and Panchenko (2016); Kordilla J. (2013); Kordilla et al. (2017), we employ a combination of kernel functions to generate a continuous function with short-range repulsive and long-range attractive components:

$$\mathbf{F}_{ij} = s_{ij} \begin{cases} (\tilde{A}\tilde{W}(r_{ij}, h_1)\frac{\mathbf{r}_{ij}}{r_{ij}} + \tilde{B}\tilde{W}(r_{ij}, h_2)\frac{\mathbf{r}_{ij}}{r_{ij}}) & \text{if } \mathbf{r}_{ij} \le h \\ \\ 0 & \text{if } \mathbf{r}_{ij} > h, \end{cases} \tag{13}$$

where $\tilde{W}$ is the cubic spline function

$$\tilde{W}(r_{ij}, h) = \begin{cases} 1 - \frac{3}{2}(\frac{\mathbf{r}_{ij}}{h})^2 + \frac{3}{4}(\frac{\mathbf{r}_{ij}}{h})^3 & \text{if } 0 \le \frac{\mathbf{r}}{h} < 0.5 \\ \\ \frac{1}{4}(2 - \frac{\mathbf{r}_{ij}}{h})^3 & \text{if } 0.5 \le \frac{\mathbf{r}_{ij}}{h} < 1 \\ \\ 0 & \text{if } \frac{\mathbf{r}_{ij}}{h} \le 1. \end{cases} \tag{14}$$

Here, $\tilde{A}$, $\tilde{B}$, h_1, and h_2 determine the shape of $\mathbf{F}_{ij}$. We set $\tilde{A} = 8$, $\tilde{B} = -1$, $h_1 = 0.5$, and $h_2 = 1$. For a given $\mathbf{F}_{ij}$ shape, s_{ij} determines the magnitude of surface tension and the static contact angle.

The parameter s_{ij} is equal to s_{ff} for the interaction between two fluid particles and s_{sf} for the interaction between fluid and solid particles. The ratio of s_{ff} and s_{sf} controls the static and dynamic contact angles. For a liquid to wet the surface, s_{ff} should be set greater than s_{sf}, and vice versa.

The SPH discretization of Eqs. (1)–(2) is:

$$\frac{d\Theta_i}{dt} = (C_{m_i} + \rho_i \mathbf{g} S e_i S_i) \frac{d\psi_i}{dt} = \sum_{j=1}^{N} 2 \frac{m_i m_j}{m_i + m_j} \frac{\rho_i + \rho_j}{\rho_i \rho_j} \cdot \mathbf{K}_s k_{r_i} (d\psi_{ij} + dz_{ij}) \cdot \frac{dW(r_{ij}, h)}{dr_{ij}}. \quad (15)$$

Here, each particle (solid and fluid) is assigned an initial water content Θ and initial pressure head ψ. The water content of a solid particle is defined as the volume of water in the particle divided by the volume of the particle. The water content of fluid particles is defined as the volume of fluid carried by the particle divided by its initial volume.

The fluid particles are initially fully saturated and are assigned $\Theta_f = 1.0$ and $\psi_f = 0.0\,\mathrm{m}$. Depending on the type of problem, the solid particles are assigned $\Theta_b = 0.0$ or Θ_b equal to a residual water content. Once fluid particles come into contact with solid particles, the exchange of fluid is governed by the Richards equation, i.e., a pressure-head-dependent transfer is established. The changes in water content and pressure head for solid and fluid particles are found using Eq. (15). The maximum Θ_b of solid particles is equal to the saturated water content of the porous matrix based on the user-defined porosity.

If the water content Θ_f of fluid particles falls below a critical threshold $\Theta_f < 0.99$, we redistribute the total water content of all particles below the threshold such that most particles are fully saturated again with $\Theta_f = 1.0$. Fluid particles that are still below the critical threshold after the redistribution are marked and removed at the end of the time step (Fig. 1). The residual water content (commonly less than the water content of one single particle) is stored and taken into account during the next time step. This procedure is is applied to all particles within a single MPI domain.

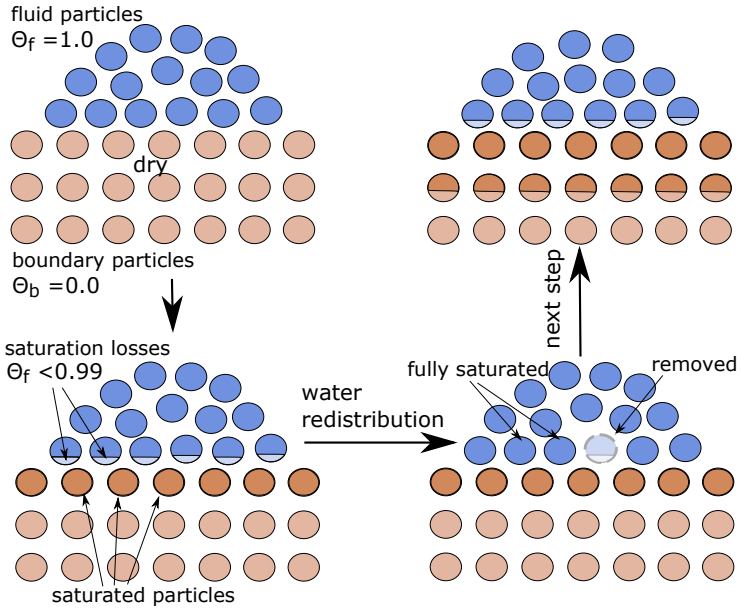

Figure 1. Particle removal algorithm.

To properly conserve the water balance in the system, we rely on the mass conservation equation:

$$\frac{\partial \Theta}{\partial t} = \nabla \cdot (\sum q_{in} - \sum q_{out}) = 0\,, \quad (16)$$

where q is the specific flux. For every time step, we calculate the sum of Θ_f and Θ_b for all fluid and boundary particles based on Eq. (17). To control the water balance in the system, the total Θ must stay constant:

$$\Theta = \sum \Theta_f + \sum \Theta_b = const. \tag{17}$$

We employ a modified Velocity Verlet time stepping scheme (Ganzenmüller et al., 2011):

$$\mathbf{v}_i(t + \tfrac{1}{2}\Delta t) = \mathbf{v}_i + \tfrac{1}{2}\mathbf{a}_i(t) \tag{18a}$$

$$\bar{\mathbf{v}}_i(t + \Delta t) = \mathbf{v}_i(t) + \Delta t \mathbf{a}_i \tag{18b}$$

$$\mathbf{r}_i(t + \Delta t) = \mathbf{r}_i(t) + \Delta t \mathbf{v}_i(t + \tfrac{1}{2}\Delta t) \tag{18c}$$

$$\mathbf{v}_i(t + \Delta t) = \mathbf{v}_i(t + \tfrac{1}{2}\Delta t) + \frac{1}{2}\mathbf{a}_i(t + \Delta t), \tag{18d}$$

where the new particle acceleration $\mathbf{a}_i(t + \Delta t)$ can be obtained using an extrapolated velocity $\bar{\mathbf{v}}_i$.

Time step constraints are given by (A. Tartakovsky & Meakin, 2005):

$$\Delta t \leq 0.25h/3c \tag{19a}$$

$$\Delta t \leq 0.25\text{min}(h/3 \mid \mathbf{a}_i \mid)^{1/2} \tag{19b}$$

$$\Delta t \leq \text{min}(\rho_i h^2/9\mu_i), \tag{19c}$$

where $\mid \mathbf{a}_i \mid$ is the magnitude of acceleration $\mathbf{a}_i$.

3 Model Validation

3.1 Constant pressure head boundary

Here we provide a validation procedure for the SPH discretization of the Richards equation applied to solid particles representing the porous matrix. We model the pressure head distribution inside a vertical porous column with a constant pressure head boundary. The dimensions of the column are 0.5×0.5×2 m. This model setup includes 38 720 solid particles, with an initial pressure head $\psi_0 = -2.0\,\text{m}$, isotropic conductivity $\mathbf{K}_s = 1 \times 10^{-4}\,\text{m}\,\text{s}^{-1}$, $S_s = 7.5 \times 10^{-5}\,\text{Pa}^{-1}$, $\Theta_s = 0.25$, $\Theta_r = 0.0$, and the van Genuchten parameters $n = 2$, $m = 0.5$, and $\alpha = 1$ (Fig. 2a). A constant pressure head boundary with $\psi_b = -0.5\,\text{m}$ is prescribed at the bottom of the domain. The particles are placed on a uniform cubic lattice with a lattice size of $\Delta x = 2.5 \times 10^{-2}\,\text{m}$. The mass and density of each particle is $m_0 = 1 \times 10^{-3}\,\text{kg}$ and $\rho_0 = 1000\,\text{kg}\,\text{m}^{-3}$, respectively. The smoothing length is set to $h = 8.55 \times 10^{-2}\,\text{m}$. This yields an average number of 40 interacting particles, which was shown to be sufficient to achieve an accurate solution (A. M. Tartakovsky & Meakin, 2005; Kordilla J., 2013; Kordilla et al., 2017). The simulation is run on 16 processors. Figure 2 shows the SPH simulation results for the pressure head inside the vertical column at 0, 1, 6, and 16 hours.

Validation is accomplished by comparison with a FEM COMSOL model. Figure 3 shows the pressure head distributions along the vertical column at 1, 6, and 16 hours for our SPH and for the COMSOL model. To quantify the difference in the SPH and COMSOL pressure head solutions, for $t = 1$, 6, and 16 hours, we calculate the standard deviation

$$s_t = \sqrt{\frac{\sum_{i=1}^{N}(\psi_{z_i}^s - \psi_{z_i}^c)^2}{N-1}}, \tag{20}$$

and standard error

$$SE_t = \frac{s_t}{\sqrt{N}}, \tag{21}$$

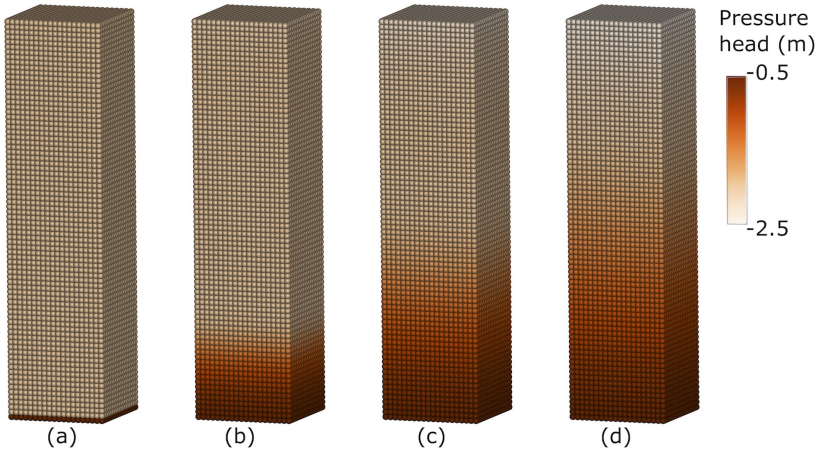

Figure 2. Pressure head distributions for a vertical column with constant pressure head boundary at different times: (a) $t_0 = 0\,\text{h}$, (b) $t_1 = 1\,\text{h}$, (c) $t_2 = 6\,\text{h}$, and (d) $t_3 = 16\,\text{h}$.

where ψ_z^s and ψ_z^c are the SPH and COMSOL pressure head solutions at distances $z =$ 0.0, 0.25, 0.5, 0.75, 1.0, 1.25, 1.5, 1.75, and 2.0 m, and the number of measurements is $N = 9$. Table 1 provides standard deviations and standard errors for $t = 1$, 6, and 16 hours. The average standard deviation is $\tilde{s}_t = 3.9 \times 10^{-2}\,\text{m}$, and the average standard error is $S\tilde{E}_t = 1.0 \times 10^{-2}\,\text{m}$, which is less than the particle spacing Δx and indicates excellent numerical accuracy of the SPH model.

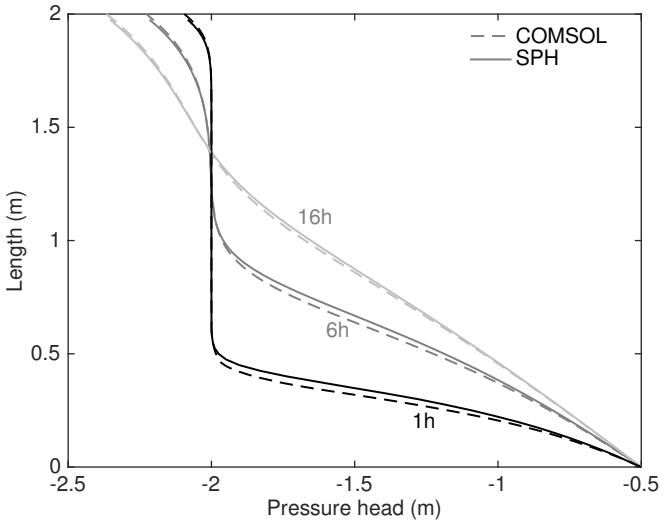

Figure 3. Comparison of pressure heads at different times for SPH and COMSOL models.

We compare our model to three laboratory experiments, (a) droplet imbibition into a porous permeable surface, (b) a flat fluid front resting on a porous permeable surface without a triple gas-solid-liquid line, and (c) a dynamic rivulet type fluid flowing on a porous surface. These three validation examples demonstrate important processes that

Table 1. Standard Deviations and standard errors of pressure heads at $t = 1$, 6, and 16 hours.

Standard deviation (m)		Standard Error (m)	
$s_{t=1h}$	3.9×10^{-2}	$SE_{t=1h}$	1.3×10^{-2}
$s_{t=6h}$	3.0×10^{-2}	$SE_{t=6h}$	1.0×10^{-2}
$s_{t=16h}$	2.1×10^{-2}	$SE_{t=16h}$	0.7×10^{-2}
$\tilde{s_t}$	3.0×10^{-2}	$\tilde{SE_t}$	1.0×10^{-2}

occur when simulating open surface, porous medium flow, and flow across the interface. The example (a) highlights the importance of proper treatment of the static triple contact line during imbibition and its effect on wetted area and static (dynamic) contact angles. Example (b) shows the ability of the model to simulate infiltration dynamics into a porous matrix for larger volumes of fluid and without the presence of a triple contact line at the solid-fluid interface. Finally, example (c) shows the ability of the model to recover the complex effects of matrix imbibition during rapid open surface flow (droplets, rivulets) and the respective outflow dynamics affected by the magnitude of retardation within the porous matrix.

3.2 Drop imbibition

3.2.1 Experimental and simulation setup

First, we study the droplet imbibition into a porous sandstone. In the laboratory experiment, a water droplet with radius 1.8 mm is placed above a slice of sandstone (type "Seeberger") at a distance of 5.8 mm between the surface and droplet center (Fig. 4a, top). The droplet size is controlled with an adjustable volume pipette. After the droplet is released from the pipette, it comes into contact with the sandstone surface and is slowly imbibed by the porous sandstone slice. During the experiment, changes in droplet size and shape are recorded with a camera with a frame rate 24 frames per second (about 1 frame every 0.04 seconds), and the imbibition time is measured.

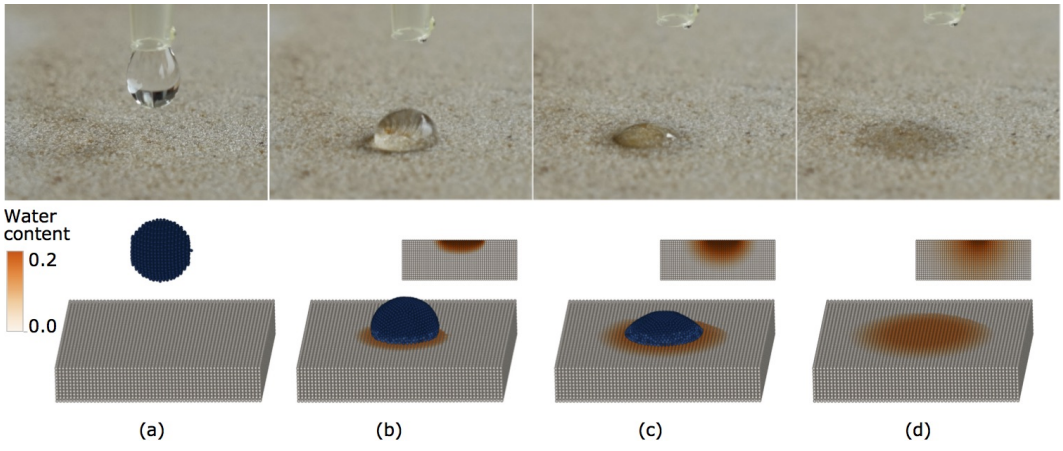

Figure 4. Experimental (top) and simulation (bottom) results of droplet imbibition and simulated infiltration front (insets) at different times: (a) before start, (b) $t_1 = 0.4$ s, (c) $t_2 = 1.84$ s, and (d) $t_3 = 2.68$ s.

The laboratory experiment is modelled by a rectangular block of solid particles that represents the sandstone slice and a sphere of fluid particles at a height of 5.8 mm above the solid surface (Fig. 4a, bottom). The dimensions of the solid block are 12×12×2 mm, and the water droplet has a radius of 1.8 mm.

Solid particles are placed on a uniform cubic lattice with a lattice size of $\Delta x = 2.0 \times 10^{-4}$ m. Each particle (solid and fluid) has a density of $\rho_0 = 1000\,\mathrm{kg/m^3}$ and a mass $m_0 = \rho_0(\Delta x)^3 = 8 \times 10^{-9}$ kg. The viscosity is set to $\mu = 1.296 \times 10^{-3}\,\mathrm{Pa\,s}$, the speed of sound to $c = 2.5\,\mathrm{m/s}$, the gravitational acceleration to $\mathbf{g} = 9.81\,\mathrm{m/s^2}$, and the smoothing length to $h = \sqrt[3]{40}(\Delta x) = 6.84 \times 10^{-4}$ m, where 40 is the particle number density, i.e., the number of interacting particles within the kernel range h. The system is resolved with 39 600 solid and 3042 fluid particles. Input parameters are: porosity ϵ_p, permeability $\mathbf{K}_s$, storage coefficient S_s, saturated Θ_s and residual Θ_r water content of the sandstone, and the van Genuchten parameters α, m, and n. These parameters can be estimated from the grain size and pore size distribution analysis of the Seeberger sandstone sample demonstrated in the following section. The simulation is run on 4 processors.

3.2.2 Parameter estimation

Effective porosity $\epsilon_p = 0.186$ of the sandstone is determined by pore size analysis based on mercury porosimetry (Fig. 5, Sustrate (2017)).

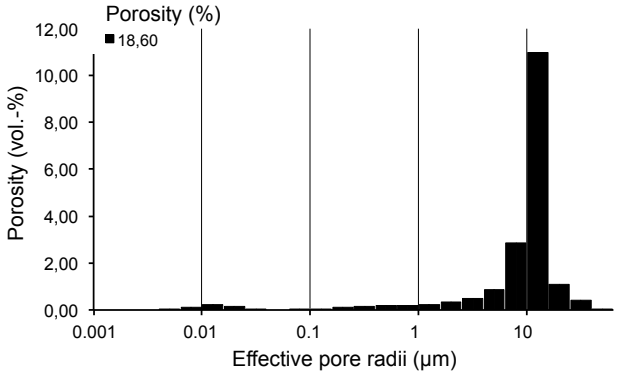

Figure 5. Porosimetry of Seeberger sandstone (Sustrate, 2017).

The (isotropic) conductivity $\mathbf{K}_s$ is estimated by Kozeny–Carmen empirical relationship (Kozeny, 1927; Carman, 1937):

$$\mathbf{K}_s = \left(\frac{\rho g}{\mu}\right)\frac{\epsilon_p^3}{(1-\epsilon_p)^2}\left(\frac{d_m^2}{180}\right). \tag{22}$$

Based on the results of a sieve analysis (Sustrate, 2017), the representative grain size was found to be $d_m \approx 0.125$ mm. Together with $g = 9.81\,\mathrm{m\,s^{-2}}$ and $\rho = 1000\,\mathrm{kg\,m^{-3}}$ the saturated hydraulic conductivity is determined with Eq. (22) as $\mathbf{K}_s = 6.39 \times 10^{-6}\,\mathrm{m\,s^{-1}}$.

The storage coefficient S_s is found from Eq. (23):

$$S_s = \epsilon_p \chi_f + (1-\epsilon_p)\chi_p, \tag{23}$$

where $\chi_f = 4.6 \times 10^{-10}\,\mathrm{Pa^{-1}}$ is the compressibility of water, and $\chi_p = 3.8 \times 10^{-6}\,\mathrm{Pa^{-1}}$ is the estimated compressibility of the porous matrix based on the porosity $\epsilon_p = 0.186$ (Hall et al., 1953). Using Eq. (23), we obtain the storage coefficient $S_s = 3.09 \times 10^{-6}\,\mathrm{Pa^{-1}}$.

The van Genuchten parameter α is found following Guarracino (2007):

$$\alpha = \Big(\frac{2\sigma cos\theta}{\rho g r_{max}}\Big)^{-1}, \tag{24}$$

where $\sigma = 0.0735\,\mathrm{N\,m^{-1}}$ is the surface tension of water at 10 °C, $\theta = 90°$ is the static contact angle of the fluid on a solid surface, $r_{max} = 15\,\mu\mathrm{m}$ is the maximum pore radius (Fig. 5, Sustrate (2017)), $g = 9.81\,\mathrm{m\,s^{-2}}$, and $\rho = 1000\,\mathrm{kg\,m^{-3}}$. Employing Eq. (24), we obtain $\alpha \approx 1.0\,\mathrm{m^{-1}}$. The parameters m and $n = [1-m]^{-1}$ are found based on the fractal dimension D (Mandelbrot, 1983; Ghanbarian-Alavijeh et al., 2010):

$$m = \frac{3-D}{4-D}. \tag{25}$$

The parameter D can be found from the mass-based relationship (Tyler & Wheatcraft, 1992; Boadu, 2000):

$$\frac{M(d<d_m)}{M_T} = \Big(\frac{d_m}{d_{max}}\Big)^{3-D}, \tag{26}$$

where d_{max} is the upper size limit of the particle sizes from the sieve analysis, M_T is the total mass of a sample, and $M(d<d_m)$ is the mass of soil with grains smaller than d_m. From the sieve analysis, we obtain $M_T = 159.0\,\mathrm{g}$, $M(d<d_m) = 17.3\,\mathrm{g}$, $d_m = 0.125\,\mathrm{mm}$, and $d_{max} = 1.0\,\mathrm{mm}$. The parameter $D = 1.93$ is estimated from Eq. (26) by log transforming both sides of the equation, Eq. (25) yields $m \approx 0.5$, and $n = [1-m]^{-1} \approx 2.0$.

3.2.3 Results

During imbibition, the contact line between droplet and surface can evolve in two different ways (Marmur, 1988; Lee et al., 2016; Siregar, 2012): (1) the contact line moves while the static contact angle remains constant, or (2) the contact line is pinned to the surface while the contact angle decreases. According to our laboratory observations, droplet imbibition into the Seeberger sandstone takes place with the pinned contact line (Fig. 4a–d, top). The contact angle in this case varies from $\theta = 90°$ to its minimum value, while the contact line diameter stays equal to 3.9 mm until the droplet is completely absorbed after 2.8 s (Fig. 4, top).

Figure 4 (bottom) shows the simulation results of the droplet imbibition at different times. Here, the fluid particles are initially fully saturated and have $\Theta_f = 1.0$ and $\psi_f = 0.0\,\mathrm{m}$, and the solid particles are initially set to $\Theta_b = 0.01$ and $\psi_b = -3.8\,\mathrm{m}$ (fitted value for the given van Genuchten parameter set). The subscripts f and b stand for the fluid and boundary particles, respectively.

To keep the contact line pinned to the surface after the droplet equilibrated on the surface, we linearly increase the interaction force s_{sf} from $s_{sf} = 0.0$ at $t_{eq} = 0.4\,\mathrm{s}$ to $s_{sf} = 1 \times 10^{-5}$ at $t' = 1.06\,\mathrm{s}$, and after t' the force s_{sf} stays equal its maximum value of 1×10^{-5}. The dynamic contact angle θ in this case decreases from $\theta = 90°$ at t_{eq} to its minimum value $\theta = 18°$ at t', and stays equal to this value until the end of the simulation (Fig. 6). The contact diameter stays equal to 3.9 mm from t_{eq} to $t' = 1.06\,\mathrm{s}$, when the droplet reaches its minimum dynamic contact angle.

The absorption time for the simulated droplet is 2.59 s, which is close to the experimental absorption time of 2.68 s.

3.3 Water infiltration into sandstone

Next, we consider the infiltration of 4.0 mL of water into a rectangular Seeberger sandstone sample. The dimensions of the sandstone block are 47.5×8.0×47.5 mm. The back, front, left, and right sides of the sample are sealed, and water is supplied to the top of the sample. During the experiment, we observe the infiltration front (Fig. 7, top) and measure the water level above the sandstone surface (Fig. 8).

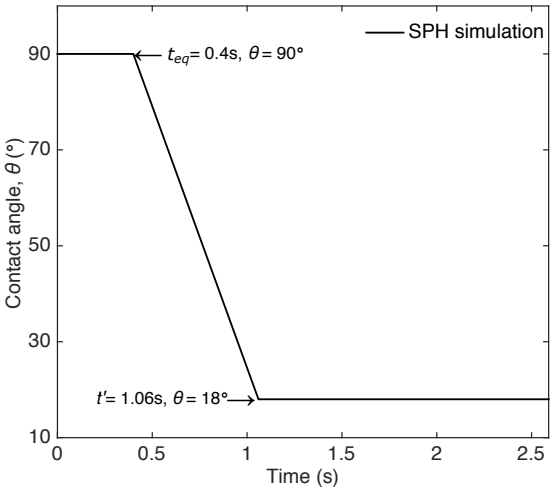

Figure 6. Changes in droplet contact angle over time.

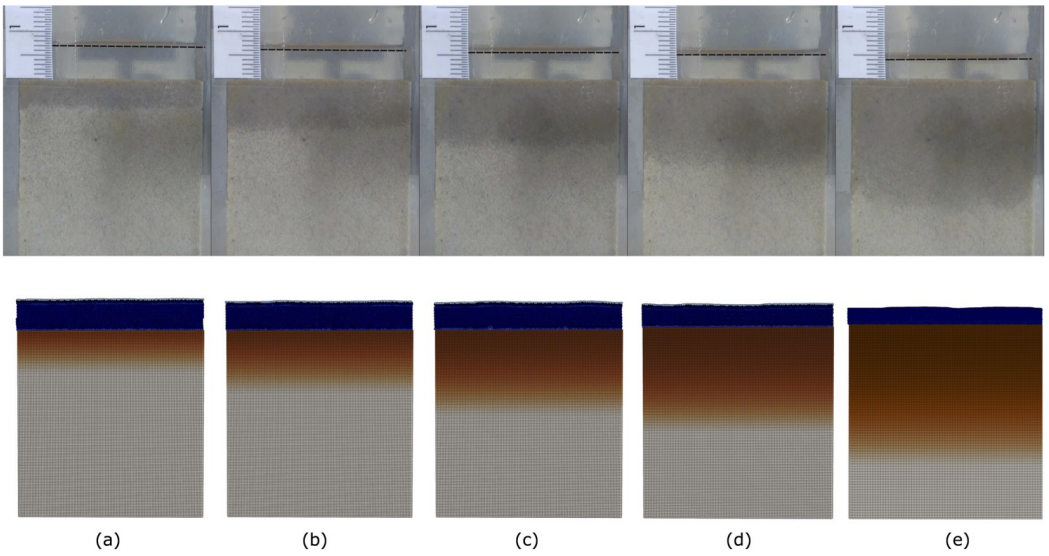

Figure 7. Comparison of experimental (top) and simulation (bottom) results of 4.0 mL of water infiltrating into a sandstone at different times: (a) $t_1 = 3$ s; (b) $t_2 = 16$ s; (c) $t_3 = 30$ s; (d) $t_4 = 50$ s; and (e) $t_5 = 100$ s.

In the simulation, we created a block of 280 840 solid particles, which are placed on a uniform cubic lattice with a lattice size of $\Delta x = 4.0 \times 10^{-4}$ m. A block of 62 500 (equivalent to 4.0 mL of water) fluid particles is placed above the solid (Fig. 7, bottom). To reproduce no-flow conditions at the back, front, left, and right side, we prescribe periodic boundaries to the direction of length and width of the sample. Mass and density of each solid and fluid particle are $m_0 = 6.4 \times 10^{-8}$ kg and $\rho_0 = 1000\,\mathrm{kg/m^3}$, respectively, and the smoothing length is set to $h = 1.37 \times 10^{-3}$ m. The viscosity is set to $\mu = 1.296 \times 10^{-3}$ Pa s, the speed of sound to $c = 2.0$ m/s, and the gravitational acceleration to $\mathbf{g} = 9.81\,\mathrm{m/s^2}$.

The parameters ϵ_p, $\mathbf{K}_s$, S_s, ψ_f, ψ_b, Θ_s, and Θ_r, and the van Genuchten α, m, and n are taken from the previous subsection. The simulation is run on 8 processors. Figure 8 compares the experimental and simulation results of the decreasing water level and wetting depth during the infiltration into the Seeberger sandstone sample. Simulation

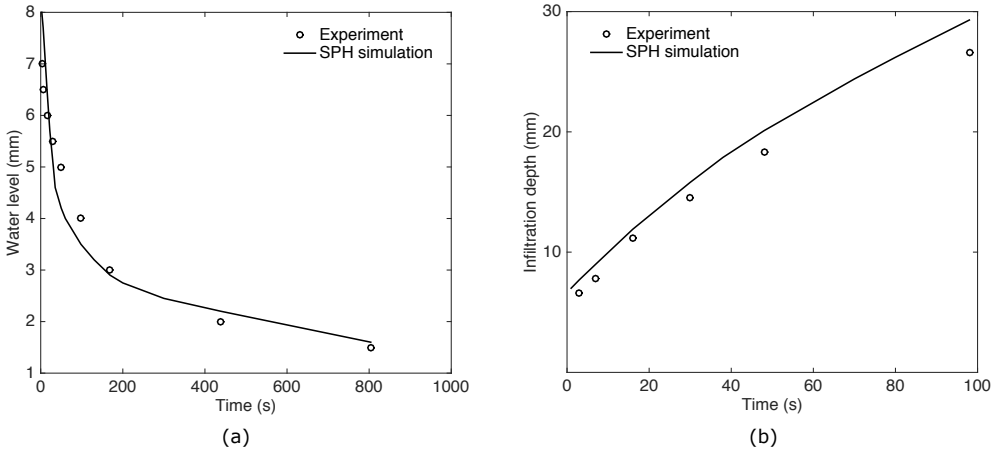

Figure 8. Experimental and simulation measurements of (a) water level above the sandstone, and (b) wetting depth during infiltration.

results are in good agreement with the laboratory experiment (Figs. 7 and 8). Small deviations between simulated and experimental results in changes of water level (Fig.8, a) can be explained by small heterogeneities in the sandstone sample and the empirical estimation of parameters based on poresize distributions in Section 3.2.2. In Fig.8(b) the simulated wetting front over time is a little bit larger than the experimental one. This deviation can be explained by boundary conditions. For the simulation, we apply periodic boundaries to the direction of length and width of the sample, which allows a uniform water infiltration in each direction of the sample. Due to the sealed back, front, left, and right sides of the sample in the experiment, the infiltration velocity is most likely slightly faster in the center of the sample due to the influence of the boundary.

3.4 Free-surface flow on a fracture wall adjacent to a porous sandstone matrix

In this section, we compare the experimental and simulation results of free-surface flows on a fracture wall and in the adjacent permeable sandstone matrix and the respective discharge rates at the outlet of the fracture.

The experimental setup consists of a Seeberger sandstone sample with dimensions 47.5×8.5× 47.5 mm, placed between two acrylic glass plates. A water inlet with a continuous water flux of $Q = 3.5\,\mathrm{mL\,min^{-1}}$ is located 5.0 mm above the upper right corner of the sandstone. A silicon rubber sheet between the acrylic glass plate and the sample prevents water flowing between the front and back side of the sample. The upper and right side surfaces are left open to allow free-surface films to evolve. During the experiment, the saturation of the porous matrix is observed (Fig. 9, top), and the water outflow mass is measured (Fig. 10).

In the SPH simulation, we create a block of 297 381 solid particles, which are placed on a uniform cubic lattice with a lattice size of $\Delta x = 4.0 \times 10^{-4}$ m. A certain amount of fluid particles (equivalent to the flux $Q = 3.5\,\mathrm{mL\,min^{-1}}$) is added at each time step

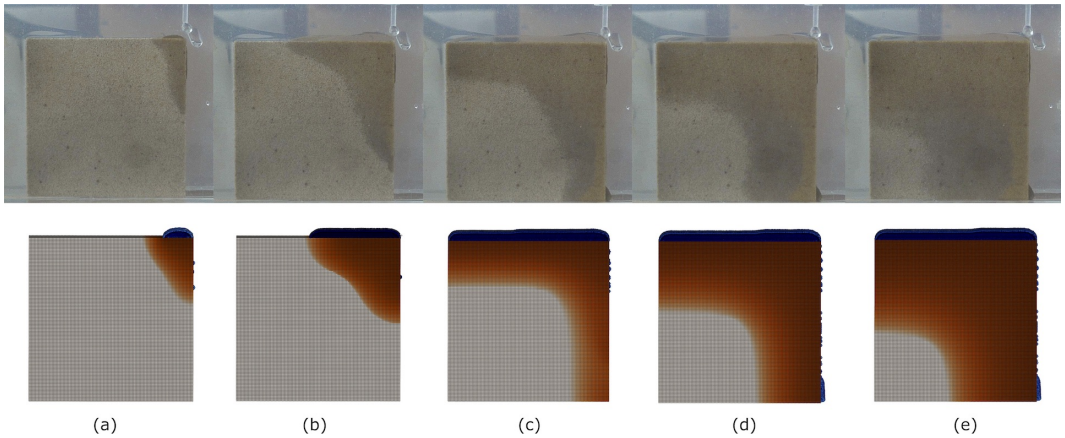

Figure 9. Comparison of experimental (top) and simulation (bottom) results of free-surface flows on a porous sandstone at different time intervals: (a) $t_1 = 5\,\mathrm{s}$; (b) $t_2 = 22\,\mathrm{s}$; (c) $t_3 = 44\,\mathrm{s}$; (d) $t_4 = 66\,\mathrm{s}$; (e) $t_5 = 110\,\mathrm{s}$.

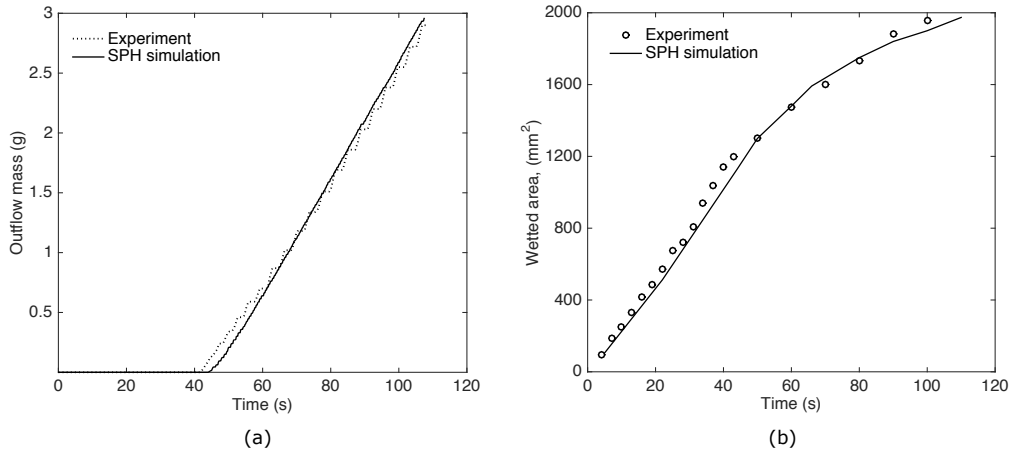

Figure 10. Experimental measurements and simulation results of (a) water outflow mass and (b) wetted area.

to the upper right corner of the solid block within a small injection volume. The simulation is run on 8 processors. The input simulation parameters are taken from the previous subsection. Figure 9 (bottom) shows the porous matrix saturation during the simulation. The experimental and simulation outflow mass measurements are shown in Fig. 10. The dotted line represents the outflow mass during the experiment, and the solid straight line represents the SPH simulation data. During the first 42 s of the experiment and 44 s of the simulation water infiltrates into the sandstone and accumulates mostly at the top of the sample, i.e., no outflow is observed. Once saturation of the sandstone reaches a critical threshold and enough water has accumulated at the top of the sandstone, rapid gravity-driven flow is initiated at the vertical surface and outflow increases nearly linearly. At this point, the system is dominated by preferential flow at the free surface, and imbibition into the porous matrix decreases slowly. The simulation results are in good agreement with the laboratory experiment, both in terms of discharge rate, as well as the onset of the initial breakthrough.

4 Preferential flow dynamics at a fracture–matrix interface

In fractured porous media in principle two flow types can be distinguished: (1) diffuse/porous medium flow, where water slowly and homogeneously saturates the porous medium, and (2) preferential flows, along macropores/fractures where water follows the path of least resistance and may bypass parts of the pore structure (?, ?). For fractured system with sufficient matrix porosity both flow types can occur simultaneously. The following section is devoted to the numerical investigation of flow type occurrence, i.e., whether preferential or diffuse flow dominates the system. Here, we consider two types of vertical fractures, one with a permeable and one with an impermeable matrix. The simulation setup consists of two blocks of solid particles separated by a 2.0 mm fracture. Each block of solid particles has a width and length of 20.0 mm, and a thickness of 2.0 mm.

The fluid is injected at a 12.0 mm distance that is measured from the fracture top with constant rates (Fig. 11). We consider 12 different injection rates, ranging from 2×10^{-8} to $2 \times 10^{-6}\,\mathrm{m^3\,s^{-1}}$.

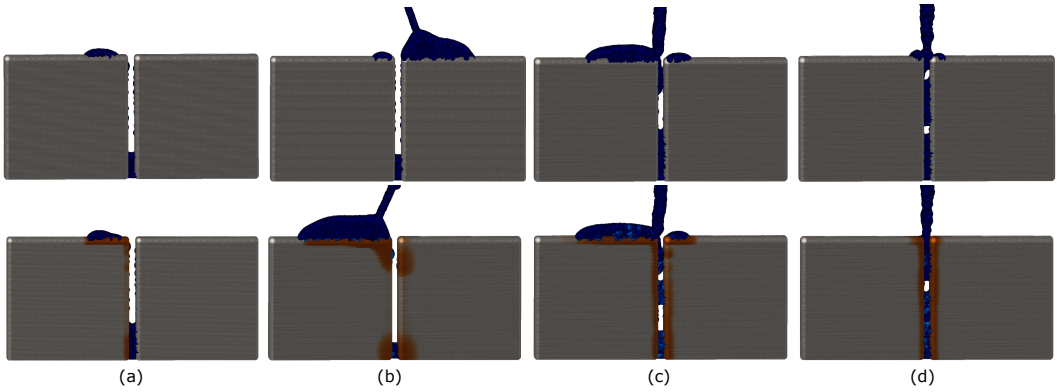

Figure 11. Infiltration dynamics in fractures with impermeable (top) and permeable (bottom) walls: (a) $Q = 2 \times 10^{-8}\,\mathrm{m^3\,s^{-1}}$, $t = 4.560\,\mathrm{s}$; (b) $Q = 8 \times 10^{-8}\,\mathrm{m^3\,s^{-1}}$, $t = 0.912\,\mathrm{s}$; (c) $Q = 6 \times 10^{-7}\,\mathrm{m^3\,s^{-1}}$, $t = 0.251\,\mathrm{s}$; and (d) $Q = 1 \times 10^{-6}\,\mathrm{m^3\,s^{-1}}$, $t = 0.228\,\mathrm{s}$.

Mass and initial density of each solid and fluid particle are $m_0 = 8 \times 10^{-9}\,\mathrm{kg}$ and $\rho_0 = 1000\,\mathrm{kg/m^3}$, respectively, and the smoothing length is set to $h = 6.84 \times 10^{-4}\,\mathrm{m}$. In the NS equations, the viscosity is $\mu = 1.296 \times 10^{-3}\,\mathrm{Pa\,s}$, the speed of sound is $c = 2.5\,\mathrm{m/s}$, and the gravitational acceleration is $\mathbf{g} = 9.81\,\mathrm{m/s^2}$. In the Richards equation, the parameters ϵ_p, $\mathbf{K}_s$, S_s, Θ_s, Θ_r, ψ_f, and ψ_b, and the van Genuchten α, m, and n are the same as described in Section 3. All simulations are run on 10 processors.

Based on the flux supplied to the fracture, the infiltration process in fractures with impermeable (Fig. 11, top) and permeable (Fig. 11, bottom) walls can be characterized according to one of the following scenarios (Fig. 12):

(1) For small fluxes $Q < 6 \times 10^{-8}\,\mathrm{m^3\,s^{-1}}$ (Fig. 11 a), accumulation of water at the top (*ponding* effect) and fracture flow occur simultaneously.

(2) For fluxes Q in the range between 6×10^{-8} and $1 \times 10^{-7}\,\mathrm{m^3\,s^{-1}}$ (Fig. 11 b), water accumulates at the top of the solid; once a sufficient quantity of water has accumulated at the top, preferential/fracture flow occurs. A similar scenario was observed during the laboratory experiment for model validation (Section 3.4).

(3) For fluxes Q in the range between 1×10^{-7} and $8 \times 10^{-7}\,\mathrm{m^3\,s^{-1}}$ (Fig. 11 c), preferential flow and ponding occur simultaneously.

(4) For large $Q < 8 \times 10^{-7}\,\mathrm{m^3\,s^{-1}}$ (Fig. 11 d), preferential flow dominates system dynamics. Once, the fracture aperture is fully saturated, ponding occurs.

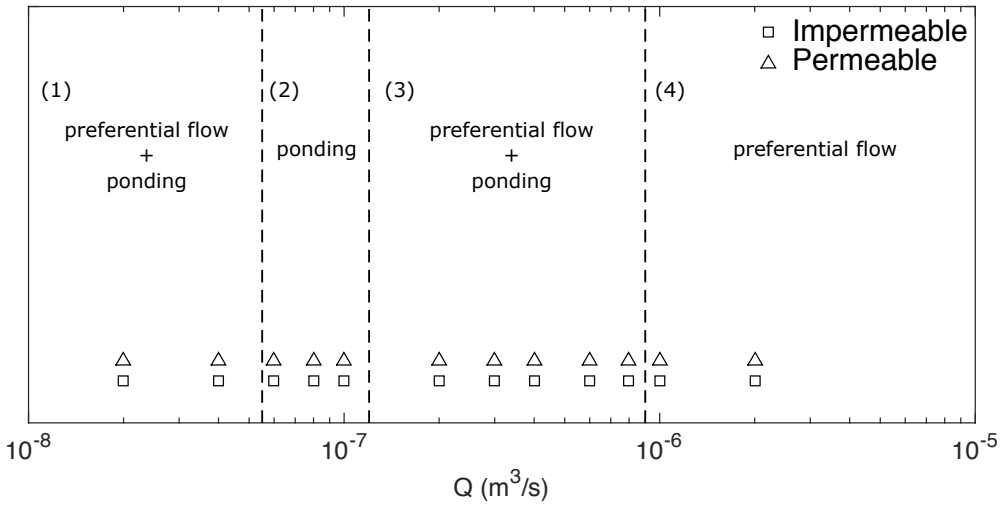

Figure 12. Four scenarios of infiltration dynamics in fractures with impermeable and permeable walls: (1) for $Q < 6 \times 10^{-8}\,\mathrm{m^3\,s^{-1}}$, preferential flow and ponding occur simultaneously; (2) for Q in the range between 6×10^{-8} and $1 \times 10^{-7}\,\mathrm{m^3\,s^{-1}}$, ponding dominates; (3) for Q in the range between 1×10^{-7} and $8 \times 10^{-7}\,\mathrm{m^3\,s^{-1}}$, preferential flow and ponding occur simultaneously; and (4) for $Q < 8 \times 10^{-7}\,\mathrm{m^3\,s^{-1}}$, preferential flow dominates.

5 Partially saturated flow in a rough walled fracture embedded in a porous medium

In the following section, we study the influence of fracture wall permeability on arrival time and on volume of water stored in the porous matrix for different infiltration rates. For the simulations, we create two rough parallel fracture surfaces separated by a 2.0 mm aperture. Each fracture surface has a width of 50.0 mm, a length of 100.0 mm, and a thickness of 10.0 mm. The roughness of the solid surface is characterized by the Hurst exponent ζ (Bouchaud et al., 1990; Shigorina et al., 2019) and an initial maximum value Δ for the random displacement from a planar surface. It was shown that ζ often assumes values of 0.80 ± 0.05 for consolidated rocks (Bouchaud, 1997; Ponson et al., 2006); however, wider ranges within $0 < \zeta < 0.9$ have been measured as well (Sahimi, 2011; Boffa et al., 1998). Here, we chose $\zeta = 0.75$ and $\Delta = 40.0$ mm. The rough fracture surfaces are resolved with 6 784 800 solid particles with a particle spacing of $\Delta x = 2.0 \times 10^{-4}$ m. Simulations are run on 32 processors. The amount of fluid particles depends on the flux Q and the simulation duration. The parameters m_0, ρ_0, h, μ, c, $\mathbf{g}$, ϵ_p, $\mathbf{K}_s$, S_s, Θ_s, Θ_r, ψ_f, and ψ_b, and the van Genuchten parameters α, m, and n are the same as described in Section 4.

We consider two types of rough fractures: (1) one with an impermeable matrix (Fig. 13, top) and (2) one with a permeable matrix in which $\mathbf{K}_s = 6.39 \times 10^{-6}\,\mathrm{m\,s^{-1}}$ (Fig. 13, bottom). Under the term *fracture wall*, we consider a thick porous (permeable or impermeable) matrix adjacent to the fracture void space. The fluid is injected along the top of the fracture with constant volumetric flux Q. Figure 13 shows the flow mode distributions inside fractures with impermeable and permeable walls for three infiltration rates: $Q = 3 \times 10^{-6}\,\mathrm{m^3\,s^{-1}}$ (Fig. 13a), $Q = 9 \times 10^{-6}\,\mathrm{m^3\,s^{-1}}$ (Fig. 13b), and $Q = 2 \times 10^{-5}\,\mathrm{m^3\,s^{-1}}$

(Fig. 13c) at arrival times for the fracture with impermeable walls. We measure arrival time as the time period between the start of the fluid injection and the time when the fluid in the fracture void space reaches the bottom of the fracture.

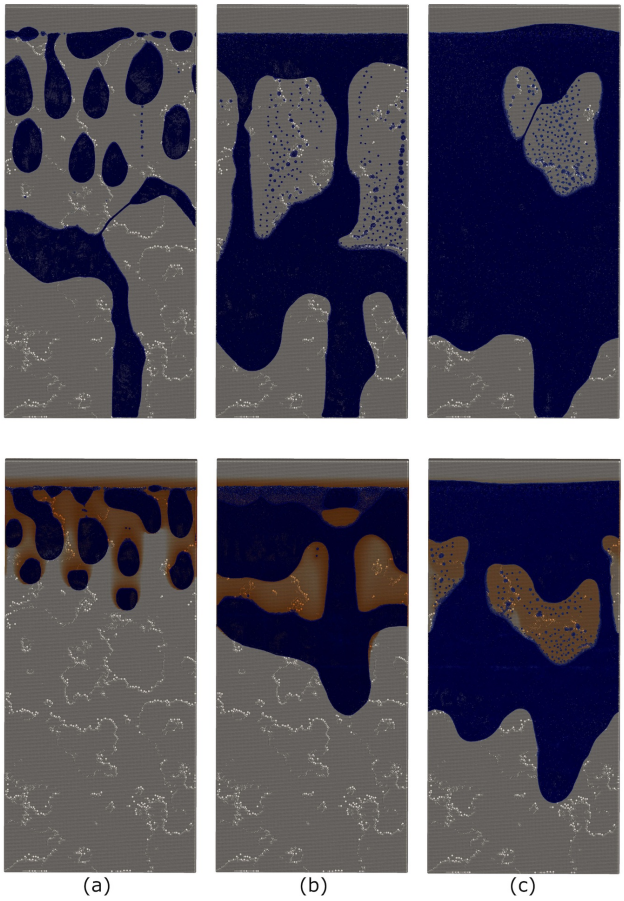

Figure 13. Flow mode distributions inside a rough fracture with impermeable (top) and permeable (bottom) walls for different fluxes at arrival times for permeable fracture: (a) $Q = 3 \times 10^{-6}\,\mathrm{m^3\,s^{-1}}$, $t = 1.026\,\mathrm{s}$; (b) $Q = 9 \times 10^{-6}\,\mathrm{m^3\,s^{-1}}$, $t = 0.570\,\mathrm{s}$; (c) $Q = 2 \times 10^{-5}\,\mathrm{m^3\,s^{-1}}$, $t = 0.388\,\mathrm{s}$.

For the lower infiltration rate ($Q = 3 \times 10^{-6}\,\mathrm{m^3\,s^{-1}}$), the dominating flow modes are droplets and a combination between temporary rivulets (slugs and elongated droplets) and snapping droplets (Fig. 9a). For the higher flow rate $Q = 9 \times 10^{-6}\,\mathrm{m^3\,s^{-1}}$, we observe a transition into a rivulet-dominated regime with the occasional (lateral) merging of rivulets. For even higher flow rates ($Q = 2 \times 10^{-5}\,\mathrm{m^3\,s^{-1}}$), flow transitions into snapping films that partially break up into rivulets.

Figure 13 (bottom) shows the saturation of the porous matrix. In contrast to simulations that employ an impermeable matrix (Fig. 13, top), a lower volume of fluid occupies the fracture void space and hence alters the flow-rate-dependent formation of flow modes. Figure 14 compares the fluid arrival times for fractures with permeable and impermeable walls. The ratios t^* between arrival times for permeable and impermeable matrix systems are listed in Table 2.

$$t* = \frac{t_{im}}{t_p}, \tag{27}$$

where t_{im} and t_p are the arrival times for an impermeable and permeable matrix, respectively. As expected, the simulation results indicate a delay in arrival time when a permeable matrix is present (Fig. 14). For an infiltration rate $Q = 3 \times 10^{-6}\,\mathrm{m^3\,s^{-1}}$, we measured a value of $t^* = 2.11$, i.e., for a permeable fracture matrix breakthrough that is about two times slower than the breakthrough for an impermeable one. For the highest infiltration rate of $Q = 2 \times 10^{-5}\,\mathrm{m^3\,s^{-1}}$, water is rapidly channeled through the fracture void space to the bottom of the fracture without any significant delay compared to a fracture with permeable walls.

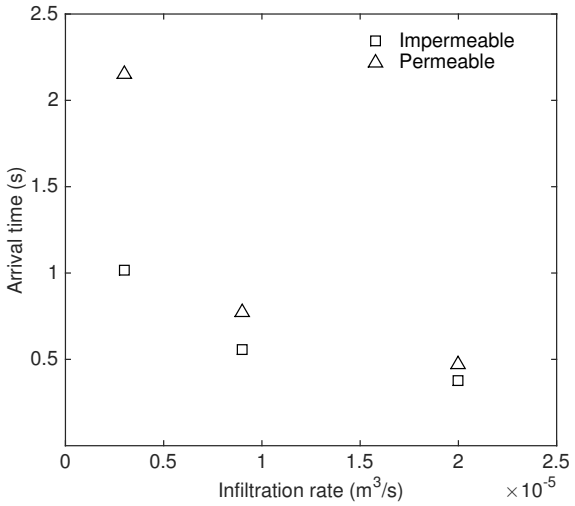

Figure 14. Dependence of fluid arrival time on infiltration rate for an impermeable and permeable matrix.

The volume of water stored in the fracture was calculated by the outflow ratio η:

$$\eta = 1 - \frac{Q_{out}}{Q}, \tag{28}$$

where Q_{out} is the volume of water leaving the system at the bottom of the fracture divided by time, and η assumes values between 0 and 1. When $\eta = 1$, no fracture outflow occurs and all of the injected water is kept in the porous matrix within the fracture void space or on the fracture surface, while a value of η close to zero represents a steady state condition where the outflow rate is equal to the infiltration rate. Figure 15 compares changes in η with time for an impermeable and permeable matrix. The difference in η between impermeable and permeable matrix systems corresponds to the relative amount of water stored in the porous matrix. Table 2 provides the difference in outflow ratio $\Delta\eta$ for an impermeable and permeable matrix at $t = 3\,\mathrm{s}$ for different infiltration rates. The largest value of $\Delta\eta_{t=3} = 0.71$ occurs at the lowest flux of $Q = 3 \times 10^{-6}\,\mathrm{m^3\,s^{-1}}$, indicating that more than 70% of water is stored within the porous matrix. For larger infiltration rates $Q = 9 \times 10^{-6}$ and $Q = 2 \times 10^{-5}\,\mathrm{m^3\,s^{-1}}$, the outflow ratio decreases with $\Delta\eta_{t=3} = 0.25$ and 0.18, respectively. Due to the limited uptake capacity of the matrix, a smaller amount of water infiltrates into the porous matrix.

6 Discussion

In this paper, we present a novel multiscale SPH model investigating preferential flow dynamics in fractures adjacent to a porous matrix. As expected flow in fractures

Table 2. Statistical properties for different fluxes in rough fractures, respectively.

Q (m^3/s)	3×10^{-6}	9×10^{-6}	2×10^{-5}
t^*	2.11	1.38	1.24
$\Delta\eta_{t=3}$	0.71	0.25	0.18

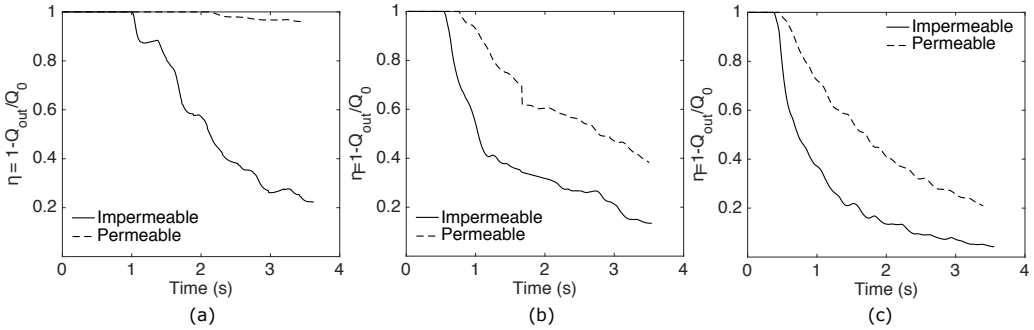

Figure 15. The outflow ratio over time for different infiltration rates: (a) $Q = 3 \times 10^{-6}\,\mathrm{m^3\,s^{-1}}$; (b) $Q = 9 \times 10^{-6}\,\mathrm{m^3\,s^{-1}}$; and (c) $Q = 2 \times 10^{5}\,\mathrm{m^3\,s^{-1}}$.

is much faster than in the porous matrix, yet flow within fractures is strongly affected by the interaction with the porous matrix and the diffuse flow component in the adjacent porous matrix.

Specifically, we study infiltration dynamics in a 2.0 mm fracture for fluxes ranging from 2×10^{-8} to $2 \times 10^{-6}\,\mathrm{m^3\,s^{-1}}$. For a given water inlet location, infiltration is characterized by one of the following four scenarios (see Figs. 11 and 12). In the first scenario (low infiltration rates of $Q < 6 \times 10^{-8}\,\mathrm{m^3\,s^{-1}}$), we observe droplet flow in the vertical fracture with some water accumulating at the top horizontal surface. In the second scenario (Q between 6×10^{-8} and $1 \times 10^{-7}\,\mathrm{m^3\,s^{-1}}$), the ponding effect dominates. In this case, water accumulates first at the top, until saturation is high enough to activate fracture flow. In the third case (Q is in the range between 1×10^{-7} and $8 \times 10^{-7}\,\mathrm{m^3\,s^{-1}}$), ponding and fracture flow occur simultaneously. As soon as fluid reaches the fracture top, it separates into two streams. One enters the fracture, while the other one connects to the horizontal top surface and feeds a growing droplet/puddle. In the last scenario ($Q < 8 \times 10^{-7}\,\mathrm{m^3\,s^{-1}}$), all water enters the vertical fracture. If the infiltration rate is high enough to fill all fracture space with water, water eventually starts accumulating at the horizontal surface. In all of these cases, preferential flow transmits water rapidly to the bottom of the fracture, while matrix flow occurs much slower than fracture flow even under saturated porous medium conditions.

Next, we investigated infiltration dynamics in rough fractures with permeable and impermeable walls. We simulate a continuous water flux supplied to the top of a fracture with 50.0 mm width, 100.0 mm length, a 2.0 mm aperture, and 10.0 mm wall thickness. The roughness of the fracture walls is characterized by the Hurst coefficient $\zeta = 0.75$ and $\Delta = 40.0$ mm. We consider three infiltration rates of $Q = 3 \times 10^{-6}$, $Q = 9 \times 10^{-6}$, and $Q = 2 \times 10^{-5}\,\mathrm{m^3\,s^{-1}}$. The simulation results show a delay in arrival times for a fracture with permeable walls as compared to a fracture with impermeable walls, especially for $Q = 3 \times 10^{-6}\,\mathrm{m^3\,s^{-1}}$ because low free-surface velocities and/or high imbibition capacity causes water to efficiently saturate the porous matrix. For $Q = 2 \times 10^{-5}\,\mathrm{m^3\,s^{-1}}$, water flows rapidly to the bottom of the fracture without any significant delay in arrival time. Under the chosen conditions and depending on the flow rate, the permeable frac-

ture walls represent an efficient storage component capable of storing more than 70% of the infiltrated water.

7 Conclusion

We developed a fully parallelized multiscale SPH model to study infiltration dynamics in porous-fractured rock formations. In our model, flow in the porous matrix is governed by the Richards (1931) equation, which is coupled to the free-surface flow in the adjacent fracture; the flow itself is governed by the Navier–Stokes equation. Inflow dynamics from the fracture into the porous matrix are realized by an efficient particle removal algorithm and a virtual water redistribution formulation in order to enforce mass and momentum conservation. The model is validated by comparison with a numerical COMSOL model and with laboratory experiments.

The SPH model for free-surface flow in fractures was proposed and validated in our previous work. To demonstrate the implementation of the Richards equation in the SPH model, we calculated the time-dependent pressure head distribution inside a vertical solid column with a constant pressure head boundary and found a good agreement with the corresponding finite element solution obtained with the COMSOL package.

The validation of infiltration dynamics, i.e., imbibition from a free-surface flow domain into the porous matrix, is carried out via comparison to three types of small-scale laboratory experiments: (1) droplet imbibition on a horizontal sandstone plate, (2) water column infiltration into a sandstone sample, and (3) discharge of free-surface flow on a porous medium. For the droplet imbibition experiment, we observe changes in droplet size and shape, and measure the imbibition time. In the second experiment, time-dependent drawdown of a water column with a total initial volume of 4.0 mL above a sandstone slice is measured, and the saturation front in the porous matrix is observed visually. In the third experiment, we consider a continuous water flux of $3.5\,\mathrm{mL\,min^{-1}}$ supplied to the top right corner of a rectangular sandstone sample. Water accumulates at the top surface and is allowed to discharge across the open right vertical surface. In order to quantify the outflow and interaction of the fluid with the porous matrix, we measure the outflow mass leaving the system and visually determine the saturation of the porous matrix. All laboratory experiments are carried out with Seeberger sandstone samples. The permeability and van Genuchten parameters of the sandstone are estimated from pore size and grain size distribution analyses. Our model is in very good agreement with all considered types of laboratory experiments.

Next, we investigate under which condition preferential flow occurs. Our simulation results show, that a preferential flow occurs simultaneously with diffuse flow and transmits water much faster, providing rapid aquifer recharge even under unsaturated and partially saturated conditions. Depending on infiltration rate and water inlet location, preferential flow, ponding, or both can be dominant in the system. For ponding-dominated systems, we observe a short delay in fracture flow. In this case, the fracture transmits water if enough water accumulates at the top of the solid surface. For preferential-flow-dominated systems, fracture flow occurs immediately, and ponding occurs only if the fracture aperture is fully saturated.

Finally, we study infiltration dynamics of rough fractures with impermeable and permeable walls. The 2.0 mm aperture fracture has a 50.0 mm width, 100.0 mm length, and 10.0 mm wall thickness. The roughness of the fracture walls is characterized by the Hurst coefficient. Using our fully coupled numerical model, we demonstrate the influence of the fracture wall permeability on the fluid arrival time for different infiltration rates, as well as on the volume of water stored in the porous matrix adjacent to the fracture. We observe that the fracture wall's permeability has a significant influence on the arrival time and outflow ratio for low infiltration rates.

Appendix A Fundamentals of Smoothed Particle Hydrodynamics method

SPH is a mesh-free Lagrangian method where fluids are discretized with a set of N points, commonly referred to as *particles*. Each particle is defined by its position $\mathbf{r}_i$, mass m_i, density ρ_i, and velocity $\mathbf{v}_i$, $i = 1, ..., N$. The solid particles do not have a physical meaning, these are computational particles that are used to prescribe boundary conditions for the SPH Navier-Stokes equation.

SPH is based on the approximation of a continuous function and its derivative:

$$f(\mathbf{r}) = \sum_j^N \frac{m_j}{\rho_j} f(\mathbf{r}_j) W(|\mathbf{r} - \mathbf{r}_j|, h), \tag{A1}$$

$$\nabla f(\mathbf{r}) = \sum_j^N \frac{m_j}{\rho_j} f(\mathbf{r}_j) \nabla W(|\mathbf{r} - \mathbf{r}_j|, h)\,, \tag{A2}$$

where the kernel $W(|\mathbf{r} - \mathbf{r}_j|, h)$ (Fig. A1) satisfies the normalization condition,

$$\int W(|\mathbf{r} - \mathbf{r}_j|, h) d\mathbf{r} = 1, \tag{A3}$$

and has compact support h (h is also called as a *smoothing length*, or *kernel length*). In the limit of $h \to 0$, W approaches the Dirac delta function $\delta(|\mathbf{r} - \mathbf{r}_j|)$:

$$\lim_{h \to 0} W(|\mathbf{r} - \mathbf{r}_j|, h) = \delta(|\mathbf{r} - \mathbf{r}_j|). \tag{A4}$$

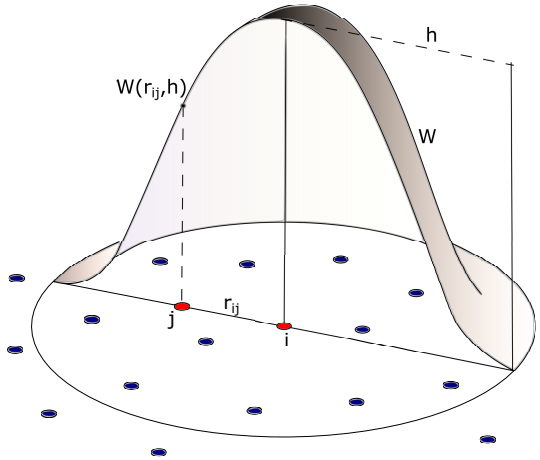

Figure A1. Kernel W with a circular support domain of length h and value $W(r_{ij}, h)$ between particles i and j at a distance r_{ij}.

A number of functional forms of W have been used in the literature. In this study, we use W in the form of a so-called "Wendland" kernel (Wendland, 1995):

$$W(r_{ij}, h) = \alpha_k \begin{cases} (1 - \frac{\mathbf{r}_{ij}}{h})^4 (4\frac{\mathbf{r}_{ij}}{h} + 1) & \text{if } 0 \le r_{ij} < h \\ 0 & \text{if } r_{ij} \ge h \end{cases}, \tag{A5}$$

where $\alpha_k = 21/(2\pi h^3)$.

The main equations, which we discretize with the PF-SPH method are the continuity equation,

$$\frac{d\rho}{dt} = -\rho \nabla \cdot \mathbf{v}, \tag{A6}$$

the momentum conservation equation,

$$\frac{d\mathbf{v}}{dt} = -\frac{1}{\rho}\nabla P + \frac{\mu}{\rho}\nabla^2\mathbf{v} + \mathbf{g}, \tag{A7}$$

and the Richards equation,

$$\frac{\partial\Theta(\psi)}{\partial t} = (C_m + \rho\mathbf{g}SeS_s)\frac{\partial\psi}{\partial t} = \nabla\cdot\mathbf{K}_s k_r(\psi)\nabla\psi + \frac{\partial K(\psi)}{\partial z}. \tag{A8}$$

The parameters are the pressure P, viscosity μ, gravity $\mathbf{g}$, water content Θ, pressure head ψ, specific storage coefficient S_s, C_m specific moisture capacity, effective saturation S_e, relative hydraulic conductivity k_r, and saturated hydraulic conductivity $\mathbf{K}_s$.

In this framework, we consider two types of particles: (1) solid/boundary particles, which represent a solid surface, fracture walls and/or porous media, and (2) fluid/water particles. The solid particles are immobile, and placed on a uniform cubic lattice with a lattice size Δx. The spacing Δx may vary depending on the simulation setup and on the required resolution. The fluid particles are initially placed on a uniform cubic lattice with the same Δx as solid particles, or they can be randomly added to the simulation domain within a defined region during the simulation. Changes in positions of fluid particles are found via an SPH discretization of Eqs.(A6)-(A7):

$$\frac{d\mathbf{r}_i}{dt} = \mathbf{v}_i, \tag{A9}$$

$$\frac{d\mathbf{v}_i}{dt} = -\sum_{j=1}^{N} m_j\Big(\frac{P_j}{\rho_j^2} + \frac{P_i}{\rho_i^2}\Big)\frac{\mathbf{r}_{ij}}{r_{ij}}\cdot\frac{dW(r_{ij},h)}{dr_{ij}} + 2\mu\sum_{j=1}^{N} m_j\frac{\mathbf{v}_{ij}}{\rho_i\rho_j r_{ij}}\cdot\frac{dW(r_{ij},h)}{dr_{ij}} + \mathbf{g} + \frac{1}{m_i}\sum_{j=1}^{N}\mathbf{F}_{ij}, \tag{A10}$$

where the density ρ_i is obtained from kernel summation as

$$\rho_i = \sum_{j=1}^{N} m_j W(\mathbf{r}_{ij}, h)\,. \tag{A11}$$

This expression conserves mass exactly and, therefore, can be used instead of the mass conservation (continuity) Eq.(A6).

The particle-particle interaction force $\mathbf{F}_{ij}$ in Eq. (A10) is used to generate surface tension and the fluid wetting behavior. Here, we use $\mathbf{F}_{ij}$ in the form (Kordilla J., 2013; Kordilla et al., 2017):

$$\mathbf{F}_{ij} = s_{ij}\Big[\tilde{A}_{ij}\tilde{W}\Big(r_{ij},\frac{h}{2}\Big)\frac{\mathbf{r}_{ij}}{r_{ij}} - \tilde{W}(r_{ij},h)\frac{\mathbf{r}_{ij}}{r_{ij}}\Big], \tag{A12}$$

where $\tilde{W}$ is a cubic spline function:

$$\tilde{W}(r_{ij},h) = \begin{cases} 1 - \frac{3}{2}(\frac{\mathbf{r}}{h})^2 + \frac{3}{4}(\frac{\mathbf{r}}{h})^3 & \text{if } 0 \le \frac{\mathbf{r}}{h} < 0.5 \\ \frac{1}{4}(2 - \frac{\mathbf{r}}{h})^3 & \text{if } 0.5 \le \frac{\mathbf{r}}{h} < 1 \\ 0 & \text{if } \frac{\mathbf{r}}{h} \ge 1 \end{cases} \tag{A13}$$

Here, s_{ij}, $\tilde{A}$, $\tilde{B}$, h_1, and h_2 are the parameters in the function $\mathbf{F}_{ij}(r)$, which combination determines the surface tension. Following (Kordilla et al., 2017), we set $\tilde{A} =$

8, $\tilde{B} = -1$, $h_1 = 0.5$, and $h_2 = 1$ and use s_{ij} as a calibration parameter to match the surface tension.

Our SPH model does not require the discretization of an air-phase, which strongly reduces computational costs, specifically when a large continuous air-phase is present. However, this also prevents the implementation of continuum surface force methods for the calculation of surface tension. Interaction forces are a suitable and efficient alternative and work for multi-phase as well as pseudo-multiphase (i.e. fluid + non-discretized airphase) problems. The exact analytical relationship between pairwise interaction forces and surface tension has been demonstrate by (A. M. Tartakovsky & Panchenko, 2016).

In our model, we have two types of interaction forces: between two fluid particles (with a coefficient s_{ff}), and between one solid and one fluid particle (with a coefficient s_{sf}). The coefficient s_{ff} is chosen in such a way, that water-air pressure difference satisfies the water surface tension. The coefficient s_{sf} controls the static contact angle of the fluid on the solid surface. As larger the s_{sf}, as more fluid attracted to the solid and as smaller the static contact angle is.

The interaction force as a function of r is shown in Fig. A2. The balance between attraction and repulsion keeps particles at a certain distance between each other.

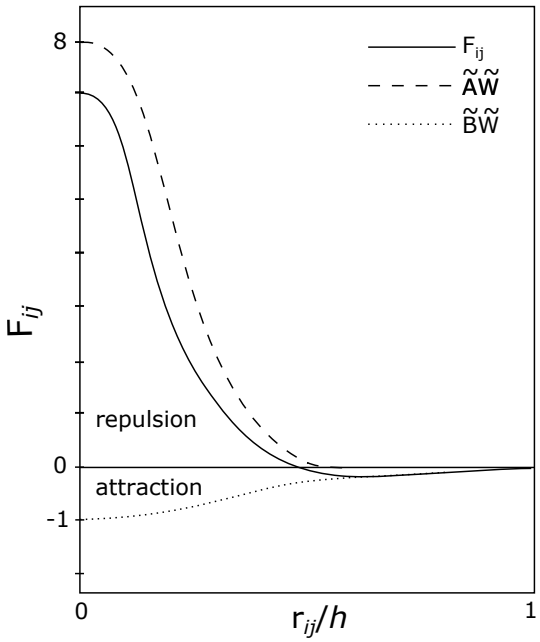

Figure A2. Interaction force between particle i and j depending on a distance $\mathbf{r}_{ij}$ between them and kernel length h.

The smoothing length h is chosen for each simulation in such a way that $h = \sqrt[3]{40}(\Delta x)$, where Δx is the particle spacing, and 40 is the particle number density, i.e., the number of interacting particles within the kernel range h, which was shown to yield sufficient numerical accuracy (A. M. Tartakovsky & Meakin, 2005; Kordilla J., 2013; Kordilla et al., 2017). The mass of each particle m_0 is set to $m_0 = \rho_0(\Delta x)^3$. Both solid and fluid particles have the same mass and volume, and hence the same smoothing length h.

Acronyms

EOS Equation of State
FEM Finite element model
LAMMPS Large-Scale Atomic/Molecular Massively Parallel Simulator
MPI Message Passing Interface
NS Navier-Stokes equation
PF-SPH Pairwise-Force Smoothed Particle Hydrodynamics
PDE Partial differential equation
REV Representative Elementary Volume

Notation

$\mathbf{a}_i$	particle acceleration
$\tilde{A}$	interaction forces coefficient
$\tilde{B}$	interaction forces coefficient
c	speed of sound
C_m	specific moisture capacity
D	fractal dimension
d_m	representative grain size
d_{max}	upper grain size limit
$\mathbf{F}$	force
$\mathbf{F}_{ij}$	interaction force acting between particle i and j
$\mathbf{g}$	gravitational acceleration
h	kernel length
i	particle index
j	particle index
k_r	relative hydraulic conductivity
$\mathbf{K}_s$	saturated hydraulic conductivity
m	van Genuchten parameter
m_0	particle mass
$M(d < d_m)$	percentage of mass less than d_m
M_{out}	outflow mass
M_t	total mass
n	van Genuchten parameter
$\mathbf{n}$	normal vector
N	number of measurements
P	pressure
q	specific flux
Q	volumetric flux
Q_{in}	inflow volumetric flux
Q_{out}	outflow volumetric flux
$\mathbf{r}$	position vector
r_{ij}	distance between particle i and j
r_{max}	maximum pore radius
S	water-air-solid contact line
s_t	standard deviation
Se	effective saturation
s_{ff}	fluid-fluid interaction coefficient
s_{sf}	solid-fluid interaction coefficient
S_s	specific storage coefficient

SE_t	standard error
t	time
t^*	ratio between arrival times
t_{im}	arrival time for impermeable fracture
t_p	arrival time for permeable fracture
$\mathbf{v}$	particle velocity vector
W	kernel function
$\tilde{W}$	interaction forces kernel function
α	van Genuchten parameter
α_k	Wendland function coefficient
γ	EOS coefficient
Δ	Hurst exponent random variance
Δt	time step
Δx	particle spacing
ϵ_p	porosity
μ	viscosity
η	outflow ratio
$\Delta\eta_{t=3}$	difference in outflow ratios at $t = 3$s
ψ	pressure head
ψ_b	pressure head of boundary particles
ψ_f	pressure head of fluid particles
ψ_d	draining pressure head
ψ_w	wetting pressure head
ρ	density
σ	surface tension
$\boldsymbol{\tau}_w$	viscous stress tensor
Θ	water content
Θ_b	water content of boundary particles
Θ_f	water content of fluid particles
Θ_r	residual water content
Θ_s	saturated water content
θ	contact angle
χ_f	fluid compressibility
χ_p	porous matrix compressibility
ζ	Hurst exponent

Acknowledgments

This work was funded by the Deutsche Forschungsgemeinschaft (DFG; German Research Foundation) under grant KO 5359/1-1 and KO 5359/4-1. A.M. Tartakovsky was supported by the Department of Energy (DOE)'s Office of Advanced Scientific Computing Research at the Pacific Northwest National Laboratory (PNNL). PNNL is operated by Battelle for the DOE under Contract DE-AC05-76RL01830. All experimental and numerical data are available online at the file repository of the University of Goettingen (GRO Data), Shigorina (2020).

References

Batchelor, G. K. (1967). An introduction to fluid dynamics. *Cambridge University Press, Cambridge, UK*.

Boadu, F. K. (2000). Hydraulic conductivity of soils from grain-size distribution:

new models. *Journal of Geotechnical and Geoenvironmental Engineering*, *126*(8), 739–746.

Boffa, J. M., Allain, C., & J.P Hulin. (1998, jun). Experimental analysis of fracture rugosity in granular and compact rocks. *The European Physical Journal Applied Physics*, *2*(3), 281–289. Retrieved from `http://www.epjap.org/10.1051/epjap:1998194` doi: 10.1051/epjap:1998194

Bouchaud, E. (1997). Scaling properties of cracks. *Journal of Physics: Condensed Matter*, *9*(21), 4319.

Bouchaud, E., Lapasset, G., & Planes, J. (1990). Fractal dimension of fractured surfaces: a universal value? *EPL (Europhysics Letters)*, *13*(1), 73.

Buscheck, T. A., Nitao, J. J., & Chestnut, D. (1991). *The impact of episodic nonequilibrium fracture-matrix flow on geological repository performance* (Tech. Rep.). Lawrence Livermore National Lab., CA (United States).

C., L. H. H. D., & S., B. G. (1998). An active fracture model for unsaturated flow and transport in fractured rocks. *Water Resources Research*, *34*, 2633-2646.

Carman, P. C. (1937). Fluid flow through granular beds. *Trans. Inst. Chem. Eng.*, *15*, 150–166.

Celia, M. A., Bouloutas, E. T., & Zarba, R. L. (1990). A general mass-conservative numerical solution for the unsaturated flow equation. *Water resources research*, *26*(7), 1483–1496.

Cockett, R. (2013). Simulation of unsaturated flow using richards equation. *Department of Earth and Ocean Science, University of British Columbia*.

Doughty, C. (1999). Investigation of conceptual and numerical approaches for evaluating moisture, gas, chemical, and heat transport in fractured unsaturated rock. *Journal of Contaminant Hydrology*, *38*(1-3), 69-106.

Fischer, U., Kulli, B., & Flühler, H. (1998). Constitutive relationships and pore structure of undisturbed fracture zone samples with cohesionless fault gouge layers. *Water Resources Research*, *34*(7), 1695–1701.

Ganzenmüller, G. C., Steinhauser, M. O., Van Liedekerke, P., & Leuven, K. U. (2011). The implementation of smooth particle hydrodynamics in lammps.

Germann, P., Helbling, A., & Vadilonga, T. (2007). Rivulet approach to rates of preferential infiltration. *Vadose Zone Journal*, *6*(2), 207–220.

Ghanbarian-Alavijeh, B., Liaghat, A., Huang, G.-H., & Van Genuchten, M. T. (2010). Estimation of the van genuchten soil water retention properties from soil textural data. *Pedosphere*, *20*(4), 456–465.

Ghezzehei, T. (2004). Constraints for flow regimes on smooth fracture surfaces. *Water Resources Research*, *40*(11).

Guarracino, L. (2007). Estimation of saturated hydraulic conductivity ks from the van genuchten shape parameter α. *Water resources research*, *43*(11).

Hall, H. N., et al. (1953). Compressibility of reservoir rocks. *Journal of Petroleum Technology*, *5*(01), 17–19.

Heilweil, V. M., Benoit, J., & Healy, R. W. (2015). Variably saturated groundwater modelling for optimizing managed aquifer recharge using trench infiltration. *Hydrological Processes*, *29*(13), 3010–3019.

Kordilla, J., Noffz, T., Dentz, M., Geyer, T., & Tartakovsky, A. M. (2017, nov). Effect of unsaturated flow modes on partitioning dynamics of gravity-driven flow at a simple fracture intersection: laboratory study and three-dimensional smoothed particle hydrodynamics simulations. *Water Resources Research*, *53*(11), 9496–9518. doi: 10.1002/2016WR020236

Kordilla J., G. T., Tartakovsky A.M. (2013). A smoothed particle hydrodynamics model for droplet and film flow on smooth and rough fracture surfaces. *Advances in Water Resources*, *59*, 1-14.

Kozeny, J. (1927). Uber kapillare leitung der wasser in boden. *Royal Academy of Science, Vienna, Proc. Class I*, *136*, 271–306.

Lee, J., Radu, A., Vontobel, P., Derome, D., & Carmeliet, J. (2016). Absorption of

impinging water droplet in porous stones. *Journal of colloid and interface science*, *471*, 59–70.

Mandelbrot, B. B. (1983). *The fractal geometry of nature* (Vol. 173). WH freeman New York.

Marmur, A. (1988). Drop penetration into a thin porous medium. *Journal of colloid and interface science*, *123*(1), 161–169.

Morris, J. P., Fox, P. J., & Zhu, Y. (1997, sep). Modeling low Reynolds number incompressible flows using SPH. *Journal of Computational Physics*, *136*(1), 214–226.

Nelson, R. (2001). *Geologic analysis of naturally fractured reservoirs*. Elsevier.

Nimmo, J. R. (2010). Theory for source-responsive and free-surface film modeling of unsaturated flow. *Vadose Zone Journal*, *9*, 295-306.

Nimmo, J. R. (2012). Preferential flow occurs in unsaturated conditions. *Hydrological Processes*, *26*(5), 786–789.

Nitao, J. J. (1991). *Theory of matrix and fracture flow regimes in unsaturated, fractured porous media* (Tech. Rep.). Lawrence Livermore National Lab., CA (United States).

Plimpton, S. (1995). Fast parallel algorithms for short-range molecular dynamics. *Computational Physics*, *117*(1), 1-19.

Ponson, L., Bonamy, D., & Bouchaud, E. (2006). Two-dimensional scaling properties of experimental fracture surfaces. *Physical Review Letters*, *96*(3), 035506.

Richards, L. A. (1931). Capillary conduction of liquids through porous mediums. *physics*, *1*(5), 318–333.

Sahimi, M. (2011). *Flow and transport in porous media and fractured rock: from classical methods to modern approaches*. John Wiley \& Sons.

Shigorina, E. (2020). *Smoothed Particle Hydrodynamics model development*. Goettingen Research Online / Data. Retrieved from `https://doi.org/10.25625/DWUV8G` doi: 10.25625/DWUV8G

Shigorina, E., Kordilla, J., & Tartakovsky, A. M. (2017). Smoothed particle hydrodynamics study of the roughness effect on contact angle and droplet flow. *Physical Review E*, *96*(3), 033115.

Shigorina, E., Tartakovsky, A. M., & Kordilla, J. (2019). Investigation of gravity-driven infiltration instabilities in smooth and rough fractures using a pairwise-force smoothed particle hydrodynamics model. *Vadose Zone Journal*, *18*(1).

Singhal, B. B. S., & Gupta, R. P. (2010). *Applied hydrogeology of fractured rocks*. Springer Science & Business Media.

Siregar, D. P. (2012). Numerical simulation of evaporation and absorption of inkjet printed droplets.

Sustrate, A.-M. (2017). *Strömungsexperimente in ungesättigten porös-geklüfteten medien: Interaktion zwischen freier oberflächenströmung und poröser matrix* (Unpublished master's thesis). Georg-August-Universität Göttingen.

Tartakovsky, A., & Meakin, P. (2005). Modeling of surface tension and contact angles with smoothed particle hydrodynamics. *Physical Review E*, *72*(2).

Tartakovsky, A. M., & Meakin, P. (2005). A smoothed particle hydrodynamics model for miscible flow in three-dimensional fractures and the two-dimensional rayleigh–taylor instability. *Journal of Computational Physics*, *207*(2), 610–624.

Tartakovsky, A. M., & Panchenko, A. (2016). Pairwise force smoothed particle hydrodynamics model for multiphase flow: surface tension and contact line dynamics. *Journal of Computational Physics*, *305*, 1119–1146.

Therrien, R., & Sudicky, E. (1996). Three-dimensional analysis of variably-saturated flow and solute transport in discretely-fractured porous media. *Journal of Contaminant Hydrology*, *23*(1-2), 1–44.

Thoma, S. G., Gallegos, D. P., & Smith, D. M. (1992). Impact of fracture coatings on fracture/matrix flow interactions in unsaturated, porous media. *Water Re-*

sources Research, *28*(5), 1357–1367.

Tokunaga, T. K., & Wan, J. (1997). Water film flow along fracture surfaces of porous rock. *Water Resources Research*, *33*.

Tsang, Y. W., & Tsang, C. (1987). Channel model of flow through fractured media. *Water Resources Research*, *23*(3), 467–479.

Tyler, S. W., & Wheatcraft, S. W. (1992). Fractal scaling of soil particle-size distributions: analysis and limitations. *Soil Science Society of America Journal*, *56*(2), 362–369.

van Genuchten, M. T. (1980). A closed-form equation for predicting the hydraulic conductivity of unsaturated soils 1. *Soil science society of America journal*, *44*(5), 892–898.

Wang, J., & Narasimhan, T. N. (1985). Hydrologic mechanisms governing fluid flow in a partially saturated, fractured, porous medium. *Water Resources Research*, *21*(12), 1861–1874.

Wendland, H. (1995). Piecewise polynomial, positive definite and compactly supported radial functions of minimal degree. *Advances in Computational Mathematics*, *4*(1), 389–396.

Zimmerman, R. W., & Bodvarsson, G. S. (1996). Hydraulic conductivity of rock fractures. *Transport in porous media*, *23*(1), 1–30.